Microseismic rupture propagation imaging

Jonas Folesky[1], Joern Kummerow[1], and Serge A. Shapiro[1]

ABSTRACT

We have developed a method for tracing the rupture propagation of microseismic events. We referred to it as *microseismic rupture propagation imaging* (MRPI), which is an adaptation of the back projection technique from global seismology. Hence, we shifted back recorded waveforms to a grid of possible source locations and obtained a coherent phase stack that migrated according to the migration of the rupture front. Using synthetic ruptures and the corresponding waveforms obtained by finite-difference modeling, we tested the viability of the approach for a reservoir model with the properties and geometry of the monitoring system of the Basel-1 geothermal reservoir. First, we found that an estimation of the rupture location, orientation, direction, and length was feasible in this environment.

The method was then applied to the four largest events ($M_L = 3.1$–3.4) recorded at the Basel-1 reservoir. We found that the obtained rupture lengths and orientations were reasonably consistent with independent estimates from seismic moments, stress drops, and fault-plane solutions. MRPI allowed us to solve the ambiguity between the actual fault plane and the auxiliary plane. The derived fault planes and rupture directions for the three best-determined events indicated that the failure process was directed preferentially from the periphery toward the injection source. This agreed with the observation that hypocenters of large-magnitude-induced events tend to occur on the edges of the stimulated volume. The results also corroborated the recently proposed idea that induced events were more probable to occur on preexisting faults if the potential rupture surface lay within the stimulated volume.

INTRODUCTION

In global seismology, tracking the rupture fronts of earthquakes with magnitudes from large ($M > 6$) to megathrust ($M > 8$) has recently become rather common. The most prominent applications are, e.g., the 2004 Sumatra-Andaman earthquake, the 2010 Maule, Chile, earthquake, or the 2011 Tohoku, Japan, earthquake (e.g., Krüger and Ohrnberger, 2005; Kiser et al., 2011, 2012; Bayer et al., 2012). A frequently used technique is to backproject the teleseismic P-wave seismograms recorded at an array or at a seismic network to a grid of possible source locations. This method is referred to as the *back-projection technique* (e.g., Ishii et al., 2007; Walker and Shearer, 2009) or the source-scanning algorithm (Kao and Shan, 2007) and is built on the constructive and destructive stack of seismic signals. It provides information on the energy release and yields estimates of rupture properties, such as direction, speed, and duration. To improve the precision, usually, coherent phases recorded by dense and large arrays are used so that different array-based time-

correction techniques can be applied. A slightly different approach is followed by Allmann and Shearer (2007), who stack local S-wave records during the $M6.0$ Parkfield earthquake, 2004, to identify a high-frequency subevent. Using back projection is a direct and elegant way to obtain independent information on the characteristics of an earthquake. One main advantage of the method is to produce an estimate of the rupture geometry without the assumption of a rupture model. To date, there is, to our knowledge, no method of imaging the rupture geometry of microseismic events. Usually, the characteristic rupture dimensions are inferred indirectly from the measured body-wave spectra, and the results depend on a specific theoretical model (e.g., Brune, 1970; Madariaga, 1976). Few studies have used the empirical Green's function method to estimate the rupture direction and rupture velocity of clustered microseismic events (e.g., Jost et al., 1998).

Here, we modify the global back-projection technique and introduce the microseismic rupture propagation imaging (MRPI). Although the key idea of MRPI is similar to back projection, it dif-

fers in one important aspect. In the microseismic domain, one often works with monitoring systems consisting of azimuthally distributed receivers, which impedes the exploitation of the waveform coherency between different receivers. Sometimes, however, one knows quite accurately the velocity structure of the reservoir and can perform high-precision event locations with arrival-time residuals as small as the sample rate (e.g., 1–3 ms in the Basel case study, Kummerow et al., 2011). This then allows very accurate stacking of seismic signals recorded by well-distributed receivers, which constitutes a condition for the MRPI method.

In this paper, we show the application of the MRPI technique to synthetic and real data at reservoir scale. Our motivation is the occurrence of relatively large, induced seismic events at several geothermal reservoirs or waste disposal sites, having magnitudes of $M_L = 3$ and greater, thus yielding rupture length estimates of up to several hundred meters (e.g., Majer et al., 2007). The quantification of source parameters, as well as their relation to injection properties might be valuable for improved hazard assessment. The largest event observed during the stimulation of the Basel-1 geothermal reservoir in 2006 was a $M_L = 3.4$ event (Häring et al., 2008). We use the configuration of the monitoring system and the reservoir properties of the Basel geothermal experiment for synthetic modeling of several ruptures and their respective wave fields. We then apply the MRPI technique to the modeled results. We finally use the MRPI to image the ruptures of the four largest real events that occurred at the Basel site. This sequence of working steps allows us to examine the general influence of station geometry and station weighting, to compare synthetic and real imaging results, and to assess the limitations of our approach.

The estimation of the source parameters, such as rupture direction and length and their relation to the injection source, will not only help to better quantify the hazard potential of reservoirs, but it will also contribute to a better understanding of rupture processes at the microseismic scale and provide a link between laboratory scale studies and regional and global-scale studies.

MICROSEISMIC RUPTURE PROPAGATION IMAGING

Methodology

Back projecting recorded waveforms from all receivers to a grid of possible source locations is a simple and very straightforward approach to unravel some of the source properties. The mathematical idea is to stack all seismograms $u(t)$ recorded at n receivers as a function of time for every ith potential source grid point, corrected by the source-receiver travel time; i.e., for the P-wave

$$s_i(t) = \sum_{k=1}^{n} \omega_k |u_k(t + t_{ik}^p + \delta t_k^p)|. \qquad (1)$$

Here, $s_i(t)$ is the stack at the ith source grid point, ω_k is a possible station specific weighting factor at the kth station, and t_{ik}^p is the predicted P-wave traveltime between the ith potential grid point location to the kth receiver location. The predicted traveltime represents the theoretical time that is needed for a seismic phase to reach the receiver depending on the actual location of the source, and it only leads to a high-amplitude stack of all contributing receivers if the respective grid point is indeed the location of the rupture front. The value δt_k^p is a time shift that corrects for the unmodeled velocity

perturbations along the raypath to receiver k. Here, it is assumed to be constant for all grid points. By iterating this stacking procedure for all possible source points and time steps, one obtains a seismogramlike trace for every grid point, containing the stacked values for each time step. One also obtains a spatial distribution of stacks of back-shifted amplitudes for each time step. The squared amplitudes of these stacks (s_i^2) are related to the released seismic energy of the source, but due to normalization and weighting at the stations, they can only be used as a proxy. This stack function will be referred to as *brightness*. For an unilateral rupture, one ideally expects to have a well-defined maximum of brightness for each time step. This peak of brightness is considered to be the rupture front at one specific point in time. The peak migrates in time as the rupture progresses in one direction. In this way, the brightness distribution potentially provides estimates for rupture orientation, direction, length, duration, and speed.

In global studies, errors of the velocity model accumulate along the travel paths from the source to the receivers at teleseismic distances. To mitigate this effect, usually, the high waveform coherency of dense array data is exploited. This allows us to determine differential traveltimes of coherent phases between the array sensors, and these are used to modify the traveltime terms in the stacking procedure in equation 1 (e.g. Ishii et al., 2007).

In microseismic monitoring with distributed receivers, waveform similarity between recorded seismograms from different receiver locations is generally not high, and one has to apply equation 1 directly. Very accurate theoretical traveltimes are required to stack the signals from different receivers correctly. This availability of accurate theoretical traveltimes is, first, a precondition for the MRPI and, second, the most significant difference to global back-projection studies. Depending on the availability and performance of the given velocity model, it may be necessary to correct the traveltimes by using station correction terms δt_k^p in equation 1. These adjustments compensate mainly for unmodeled velocity heterogeneity along the path from the microseismic event cloud to the individual receivers.

In the Basel case, we use a two-layer velocity model (Häring et al., 2008) and the station correction terms calculated from averaging the residuals of the whole microseismic event cloud (Kummerow et al., 2011). Using those in combination with high-precision P- and S-arrival times leads to average arrival time residuals of the order of 1–3 ms for the observed microseismic events (Kummerow et al., 2011). Hence, the corrections are sufficiently precise to apply the stacking according to equation 1.

We must also correct for the influence of the specific station geometry of the microseismic monitoring system. This is achieved by a weighting scheme that defines the ω_k in equation 1. In our case, a straightforward way to address this is the computation of the relative azimuth between each contributing station and the hypocenter location. The weighting assigned to each single station is the sum of half of the azimuth differences to its respective neighbor stations. In this way, the influence of an asymmetric receiver distribution with respect to the hypocenter location can be decreased significantly. For each station, we compute the Euclidean sum from the three seismogram components for the P-phase window, and we then normalize the sum trace by its maximum. Next, we apply the station-dependent time shift using static station corrections. We also include an additional phase shift for each trace, which corrects

the first location of the focus of brightness depending on an a priori hypocenter location, obtained from P- and S-wave arrival-time inversions. The maximum allowed phase shift is given by the difference of the P-pick time and the first amplitude peak in the P-phase. In our case study in Basel, this difference is up to a few tens of milliseconds. The stacking is performed using equation 1 including the weighting factors explained above. As described, we track the peak of the brightness for each time step and define it as the track of the migrating rupture front. Using the P-phase and considering the relatively small aperture layout of the receivers with respect to the source, the depth resolution is not sufficient to resolve the depth migration of ruptures of microseismic dimension, especially as we cannot make use of waveform coherency as in e.g., Ishii et al. (2007). Hence, we restrict the MRPI to the horizontal plane fixed at hypocenter depth, which means that we recover the rupture projection on this plane. This approach is also supported by the predominantly strike-slip mechanisms found for the largest earthquakes at Basel by Deichmann and Giardini (2009).

SYNTHETIC DATA

Modeling

We use the finite-difference code Evamod (Saenger et al., 2000) to model seismic sources and their respective wavefields. Evamod allows us to place different sources at different times in a defined model space. To simulate a small event (point source), we define one location and a source type and compute the elastic wavefield, which is recorded by synthetic receivers. To model a propagating rupture, we put a straight line of sources in short horizontal distances next to each other, firing one after another. The resulting wavefield of a 200-m-long, unilateral, west–east-breaking rupture is shown in Figure 1. Note the strong directivity character.

Our model grid consists of 800^3 points and a grid spacing of 10 m. Multiple geophones can be placed at any location within the grid. We use a homogeneous, isotropic model with $V_P = 5940$ m/s, $V_S = 3450$ m/s, and $\rho = 3000$ kg/m^3, which are averaged values for the geothermal reservoir at Basel, Switzerland (Häring et al., 2008). The source time functions are Gaussian pulses with a central frequency of 20 Hz for each single source. The source type is explosion. This is sufficient for our rupture modeling. A more complex radiation pattern would be eliminated by trace normalization and station weighting (compare equation 1). To model a 200-m-long rupture, 11 explosion-type sources are used, which are horizontally offset by 20 m.

Rupture models

We first show synthetic tests for two horizontal ruptures imaged with full azimuthal coverage and then for three synthetic events imaged with the irregular Basel station configuration (cf. Figure 2). The events are placed at a depth of 4000-m below the surface, which corresponds to the open-hole section of the borehole and to the center of microseismicity in the reservoir (Häring et al., 2008). Because the analysis is restricted to a fixed depth (i.e., the hypocenter depth), we only model horizontal ruptures.

Full-azimuthal coverage

The first set of ruptures is surrounded azimuthally by 16 evenly distributed stations, which are located at a horizontal distance of 2500 m at 1000-m depth. The first rupture is unilateral and breaks horizontally from west to east and has a length of 200 m. The sec-
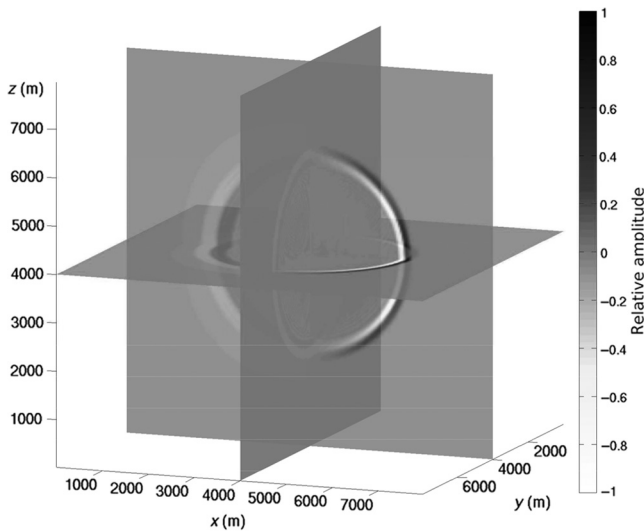

Figure 1. Snapshot of the *x*-component of the wavefield of an unilateral 200-m-long rupture, breaking from the west toward the east (corresponds to increasing *x*-values), illustrating the modeled directivity effect: The phase length and amplitude values vary strongly with the angle relative to the rupture direction (compare to the Doppler effect).
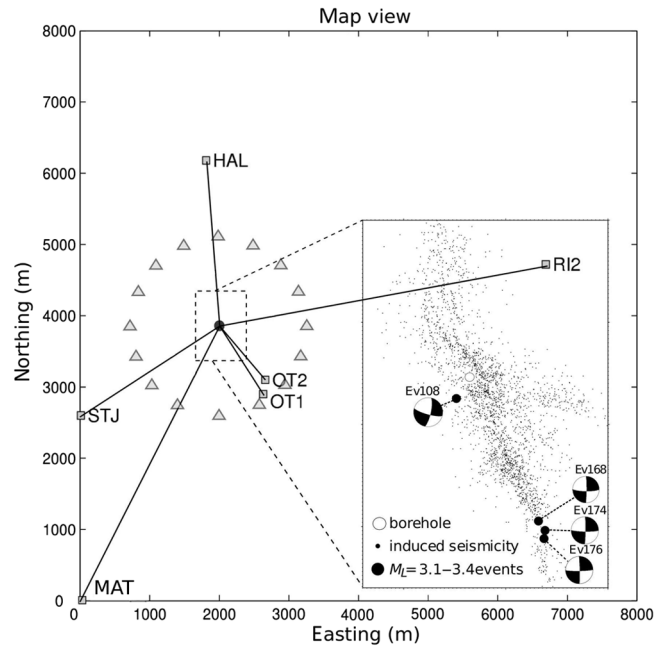

Figure 2. Basel station configuration with the borehole location in the center and study area indicated by the dashed square. The stations are weighted according to their relative azimuth coverage with respect to the source. The enlarged view shows the borehole location, the seismicity cloud, and the fault-plane solutions for the four largest events from the Basel site. The triangles illustrate a perfect station layout for some of the synthetic ruptures. However, receiver-station distances are shortened in the figure by a factor of two for visual composition.

ond rupture is a bilateral rupture nucleating at its center. It ruptures in the west and east directions, where each rupture leg is of 100 m length. MRPI snapshots of both ruptures for different time steps are shown in Figure 3. The brightness maxima are tracked as described and shown in Figure 4. The points with the highest brightness values at each time step represent the rupture path and are color coded with respect to their temporal occurrence.

The unilateral rupture is well recovered by the MRPI. The results show the rupture origin at the true location (black star in Figure 4, top left) and an eastward rupture migration at a length of 200 m. The hypocenter matches exactly with the modeled hypocenter location, and the direction of the rupture and its length are also precise. It should be mentioned, however, that the estimate of the rupture length is sensitive to the threshold value used (here, we use 66% of the maximum value for the synthetic models; see Figure 4). From all our synthetic models, we find that the rupture length tends to be underestimated.

The second rupture is bilateral. Again, we get the exact hypocenter and rupture orientation (Figure 4). The rupture directions and the lengths of the two rupture legs are correctly imaged to be 100 m in the east and west directions, respectively. Because the modeled rupture speed of both models was set as equal and the rupture dimensions are the same as for the unilateral rupture, the brightness stacks are very similar. A much shorter high-coherency phase (width of the brightness track) for the smaller bilateral rupture could be expected. However, the smearing due to the opposite directivity of the two rupture legs widens the time window of high coherency. Note that the final track of the bilateral event (Figure 4) is accurate, but it shows no migration of the center of brightness until about half of the rupture duration. Hence, the dynamic is not captured accurately, but the orientation and dimension are well resolved.

Realistic azimuthal coverage

In the next step, we consider a realistic station distribution. We use the Basel station distribution shown in Figure 2 with six distributed receivers to model three different microseismic events (a

point source, a north–south-breaking rupture, and a west–east-breaking rupture).

The resulting rupture tracks are displayed in map view in Figure 5. The black points represent the time steps, when the brightness maximum exceeds the threshold value, and the gray points are
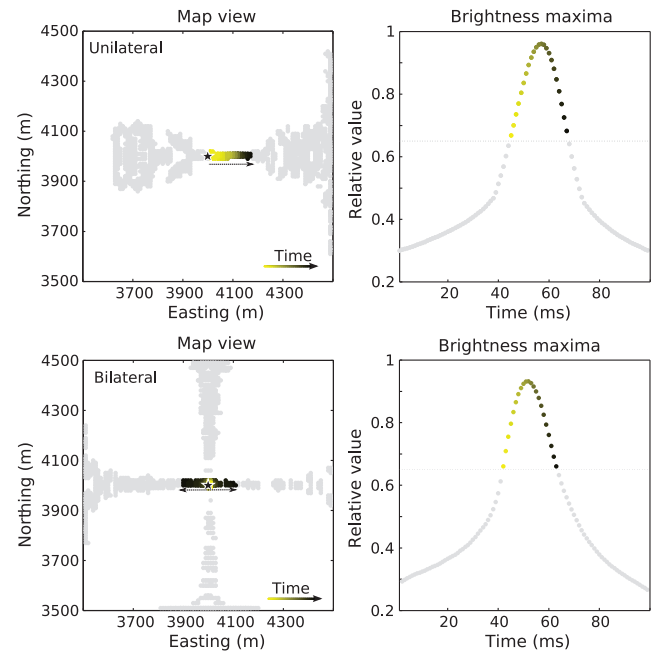

Figure 4. (Top) Rupture track and brightness maximum values over time corresponding to a 200-m west–east-breaking unilateral rupture. The color coding left and right correlates. The star is the nucleation point. The arrow shows the rupture direction. Time snapshots for that rupture are shown in Figure 3a. For the color-coded points, the amplitude of the stacked phases is above the threshold and the rupture is tracked. (Bottom) Track of a bilateral rupture and brightness maxima. The corresponding snapshots are shown in Figure 3b.
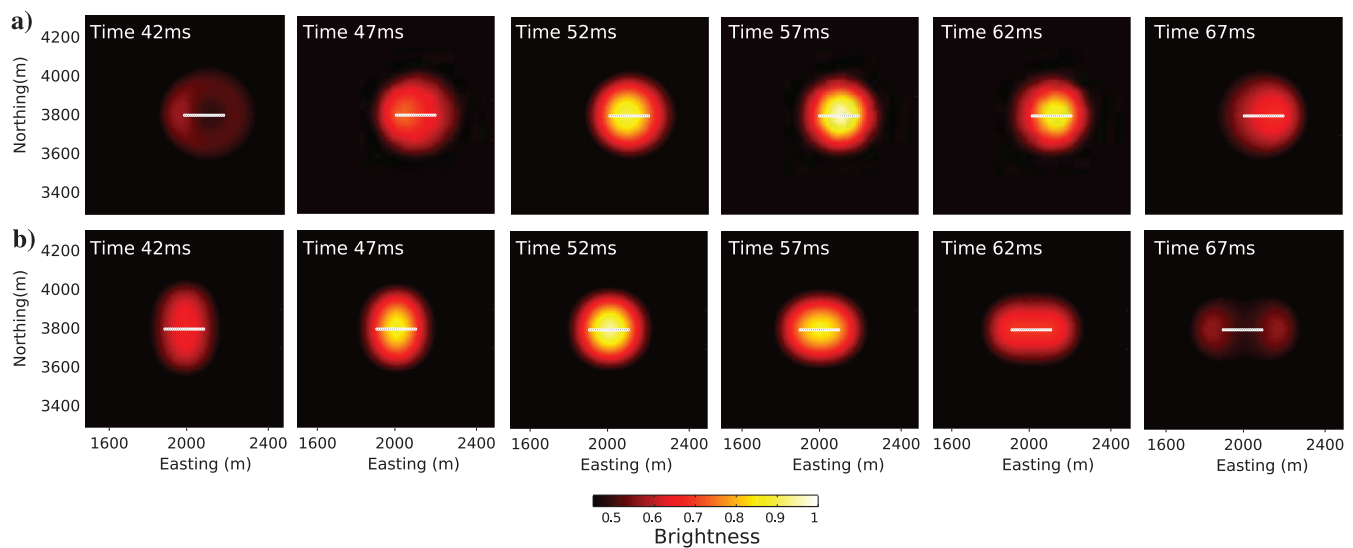

Figure 3. MRPI snapshots for six time steps for a west–east-breaking unilateral rupture (a) at the top, and a bilateral rupture (b) at the bottom. The white dots represent the modeled rupture path. The migration of the center of the bright spot represents the migration of the rupture front.

associated with small brightness values. The brightness level before and after the rupture, i.e., the coincidental summation of the projected amplitudes, is related to the site-specific geometric distribution of the receivers. The threshold is an empiric value, and it relies on several factors such as the number of contributing stations and the signal-to-noise ratio (S/N) of the seismogram traces.

The first of the modeled events (Figure 5a) is a point source, which simulates a very small microseismic event. The rupture track shows no artificial migration and is limited to the true hypocenter location (the black star in Figure 5a).

The second event (Figure 5b) is a north–south-breaking rupture of 200-m length. The MRPI technique works stably and clearly distinguishes the rupture trend from the rest of the stacked energy in the target area. The location of the rupture nucleation almost coincides with the modeled hypocenter location. The estimated rupture size of 180 m is close to the value of the model (200 m). The orientation, however, varies by approximately 25° from the original model as a consequence of the irregular and sparse station layout.

Figure 5c shows the third rupture, which breaks from the west toward the east. The difference to the north–south-breaking rupture is clearly resolved. In this case, the hypocenter is found precisely at the modeled position. The imaged rupture length is again slightly underestimated (180 m compared with 200 m in the model). The orientation also deviates by approximately 25° from the true orientation.

The comparison shows that the rupture parameters are recovered reasonably well in all three cases, but the rupture orientation is biased due to the limited azimuthal station coverage.

REAL DATA

The Basel enhanced geothermal system (EGS) data set has been described in detail by Häring et al. (2008). The microseismic cloud consists of more than 2800 located events, which are recorded by six downhole receivers distributed as shown in Figure 2. Different location studies based on the inversion of P- and S-wave arrival times consistently found a subvertical, north–northwest/south–southeast orientation of the seismicity distribution, which coincides with the direction of the maximum horizontal stress, SH_{max} (e.g., Häring et al., 2008; Dyer et al., 2010; Kummerow et al., 2011). The largest events occurred during and after the late phase of the injection experiment and finally led to its termination. Deichmann and Giardini (2009) find that nearly all of the large events were situated at the outer rim of the actual extent of the microseismic cloud and that they show mainly strike-slip mechanisms.

For this work, we have analyzed the waveforms of the four largest, $M_L = 3.1$–3.4 events. We have also tested the method for smaller ($M < 3$) events, but we did not obtain coherent results. The rupture lengths become too small to be resolvable. In the Basel case, the minimum magnitude for applying our imaging method is approximately $M = 3$, and this value is clearly related to the setup (the source-receiver distance, aperture, frequency band of the waveforms, and S/N).

The respective fault-plane solutions and locations of the four events are shown in Figure 2. We use the same two-layer velocity model and static station corrections as in the studies by Häring et al. (2008) and Kummerow et al. (2011). The hypocenter locations
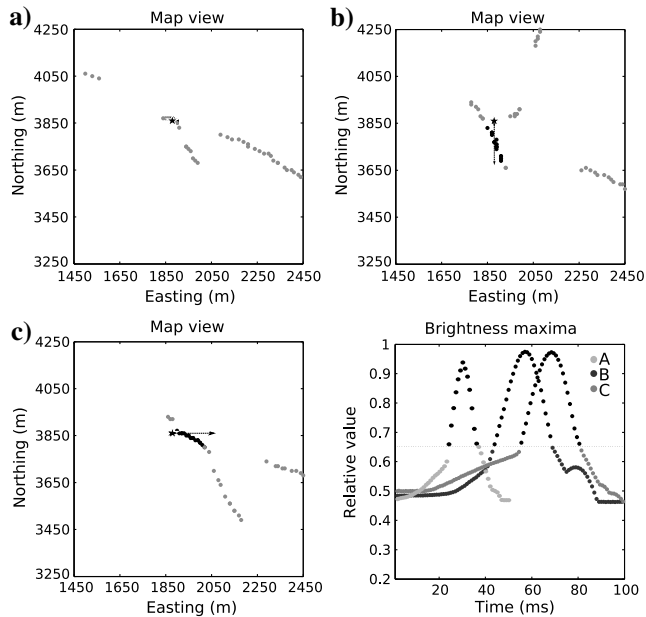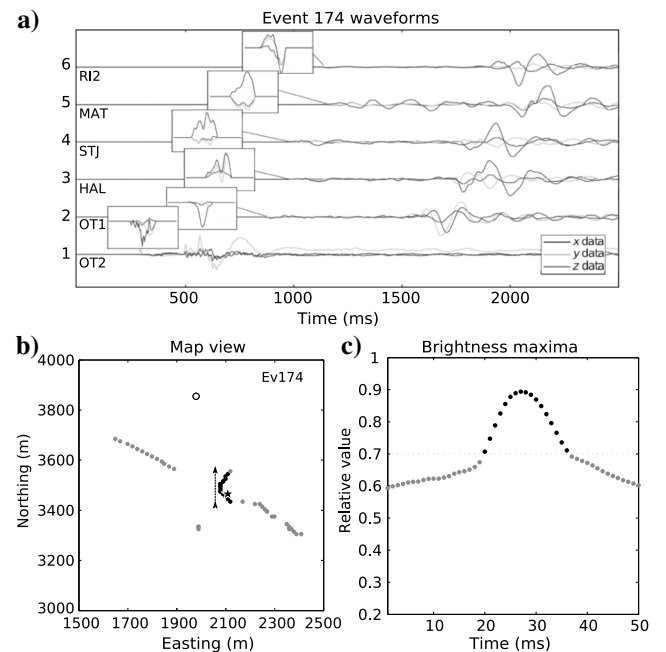
Figure 5. Horizontal rupture tracks and the corresponding brightness histories for three different synthetic ruptures using the sparse network geometry of the Basel case study. (a) MRPI results for a point source, (b) for a 200-m-long north–south-breaking rupture, and (c) for a 200-m-long west–east-breaking rupture. The black points show the spatiotemporal migration of the maximum brightness, which is interpreted as the migration of the rupture front. The gray points represent pre- and postrupture brightness. The black star is the independently obtained hypocenter location. The arrow indicates the rupture direction.

Figure 6. (a) Displacement waveforms for the Basel event $Ev_{174}(M_L = 3.2)$ recorded at six downhole instruments at the locations shown in Figure 2. The P-phase display is increased. Station OT2 is situated in the crystalline basement, and it shows a higher frequency content. (b) Rupture track. The black track points represent the rupture path. The star is the hypocenter and the circle is the borehole. (c) Temporal evolution of the maximum value of brightness for the same event.

found therein are taken as reference hypocenters. The waveforms for an exemplary event Ev_{174} are shown in Figure 6a (using the event nomenclature of Deichmann and Giardini, 2009).

Results

We apply the MRPI technique to the four largest events from the Basel experiment, and we show the complete results for the event Ev_{174} ($M_L = 3.2$) in greater detail. The large events in the Basel reservoir show unilateral behavior, and we only track a single maximum per time step and define this as the rupture front at this particular time step. The threshold, whose excess defines the rupture length, is now chosen manually at a value of 0.7, where the slope of the brightness function steepens abruptly. If the brightness does not focus as clearly as it does here, the picking of a threshold value may become impossible or involve large uncertainties of the derived rupture parameters. One reason for such an observation could be, for example, a more complex rupture behavior than unilateral or bilateral. In our case, however, the rupture of event Ev_{174} is well defined by the brightness function appearing between the imaging time steps of 18 and 38 ms (Figures 6c and 7). The corresponding positions are shown in the map view of Figure 6b. The first location is the black point that lies farthest in the south, and the rupture front then migrates from south to north. The rupture nucleation point matches the hypocenter location. The length of the rupture is approximately 150 m. The gray tracking points, before and after
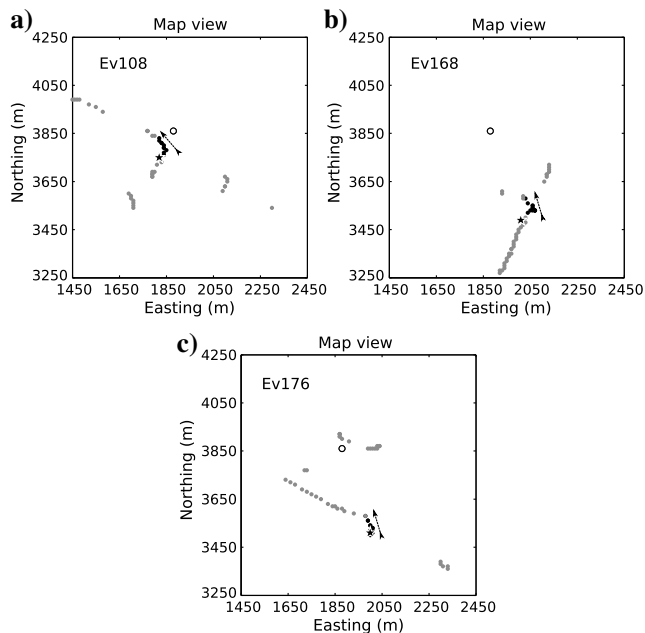
Figure 8. Same as Figure 6b, but for events (a) Ev_{108}, (b) Ev_{168}, and (c) Ev_{176}. Estimated rupture direction for events Ev_{168} and Ev_{176} is south–southeast to north–northwest and for event Ev_{108} southeast to northeast.
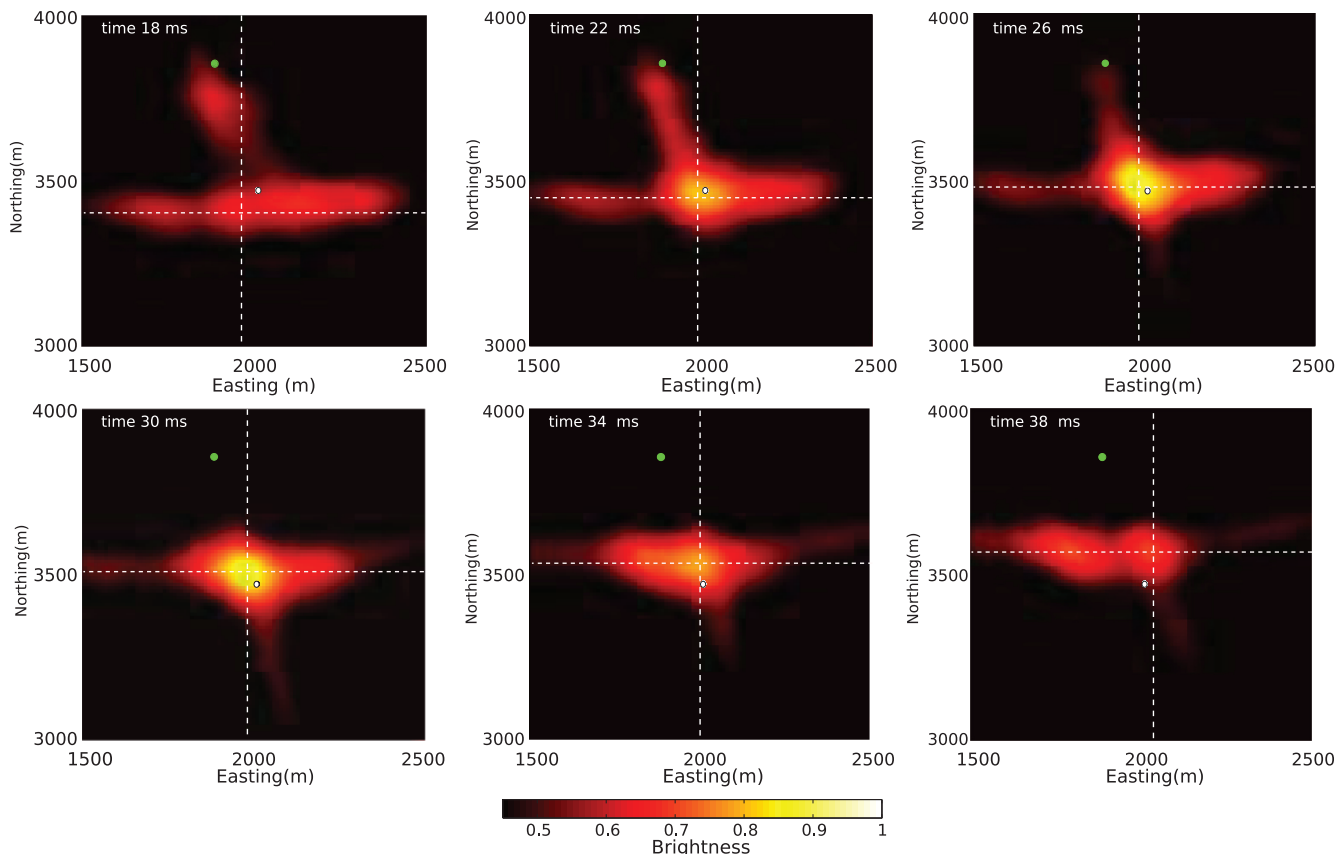
Figure 7. MRPI snapshots for the times 18–38 ms for Ev_{174}. The brightness focus position is indicated by the crossing of the white dotted lines. Its motion is considered to be the migration of the rupture front. The green circle is the borehole, and white is the (first-arrival based) hypocenter location. The corresponding rupture path is shown in Figure 8.

the defined rupture time interval, show a general trend that strongly depends on the station geometry of the site and is not related to the physical rupture. For the Basel setup, this track mostly starts in the south–southeast and migrates toward the north–northwest. The trend changes when the backshifted phases of the different receivers start to coincide, and the brightness value exceeds the threshold value. Figure 8 shows that the results for the other ruptures are generally similar. We find south–north rupture directions for the events Ev_{168} and Ev_{176} with rupture lengths of 120 m. Event Ev_{108} seems to have a slightly different rupture orientation (southeast to northwest).

For all four ruptures, we find coherent brightness maxima for a similar duration localized close to the hypocenter location covering an area of similar size. The consistency of the results for the four events with similar magnitudes and source mechanisms increases our confidence in the validity of the method.

DISCUSSION

The imaged rupture nucleation points for the synthetic ruptures coincide with the true positions of the modeled hypocenters almost perfectly. In the real data case, the offset between the imaged nucleation points and the reference hypocenters (from the arrival-time-based location study by Kummerow et al., 2011) is in the range of tens of meters. We address the offset primarily to the differences of the location method and the MRPI. Although the first method uses the first onset of the seismic phases, the MRPI is more sensitive to the higher amplitudes following the first onsets.

Using MRPI, the rupture orientation is very well recovered for a good azimuthal station coverage and it loses precision when a sparse monitoring network is used (compare Figures 4 and 5). For the Basel case, we find deviations of up to 25° in the synthetic analysis. For the real ruptures shown in this study, the imaged orientations are in the south–southeast/north–northwest direction, close to the north–south-striking nodal planes found by Deichmann and Giardini (2009) from fault-plane solutions for the same events (Figure 2). Thus, the MRPI results suggest that the north–south-striking nodal planes are the actual fault planes.

In this study, we find approximate rupture lengths of 120–150 m. We compare this with estimates computed assuming a circular fault (Eshelby, 1957) and a rectangular fault (Knopoff, 1958). Taking the stress drop value of 10 MPa, which was found (by Goertz-Allmann et al., 2011a) to be representative for the region of the largest events at the rim of the microseismic cloud at Basel, and using the conversion relation by Goertz-Allmann et al. (2011b) for local to moment magnitudes, we obtain rupture radii of approximately 100–
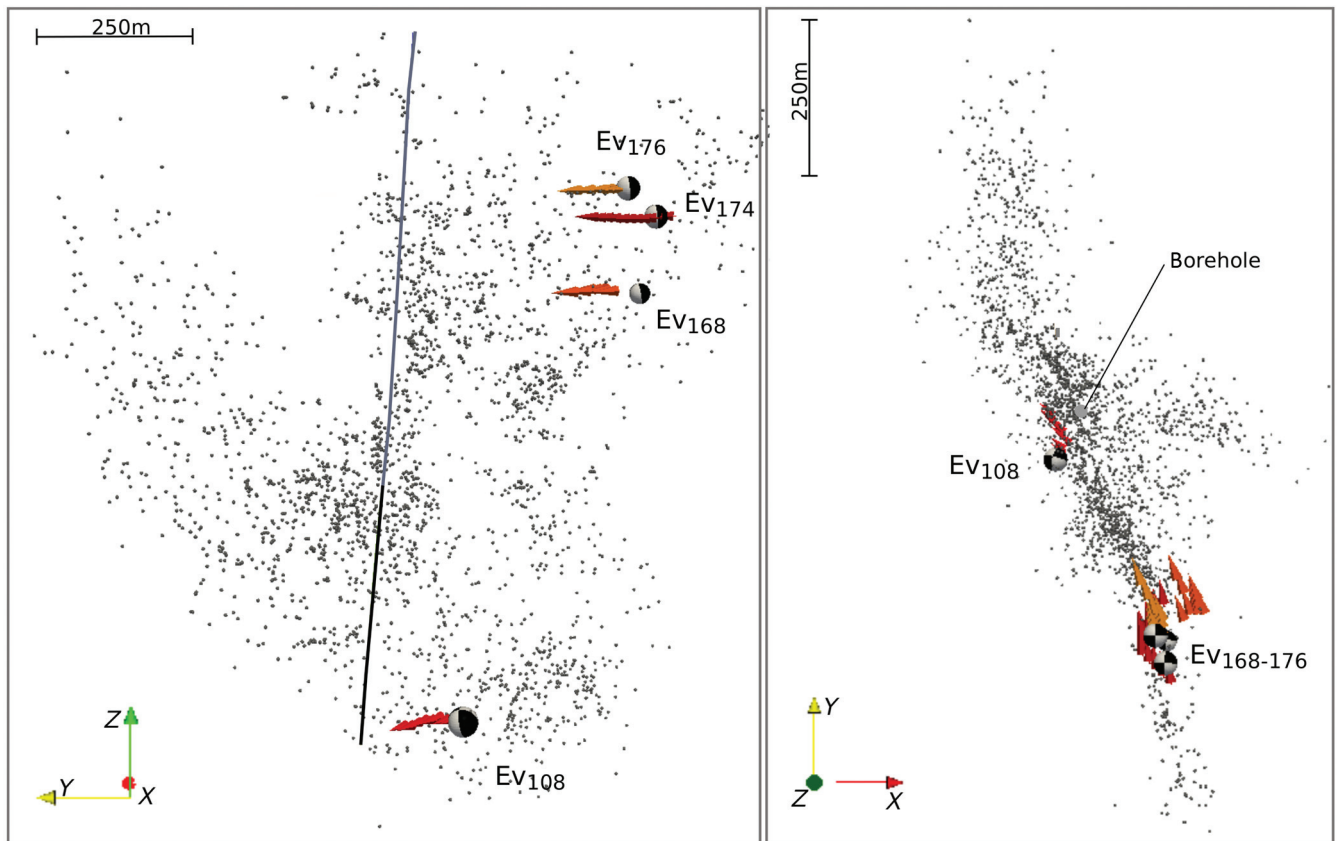

Figure 9. Basel microseismic cloud from (left) side and (right) map view. The borehole is the thin blue line, and the open hole section is black. The small gray dots represent microseismic event locations. The fault-plane solutions by Deichmann and Giardini (2009) for the four largest events are shown at their hypocenter locations. The respective rupture tracks are shown as arrows in reddish colors. Notice that the rupture tracks for all events are consistent with the shape of the seismic cloud. The rupture directions match the fault-plane solutions reasonably. Only Ev_{108} shows a deviation between the rupture orientation and the orientation of the possible fault plane of approximately 25°. The others fit significantly better. Notice that with the application of MRPI, the ambiguity of the fault-plane solutions can be solved. Also, note that all rupture directions point toward the injection well.

150 m and rupture lengths of approximately 130–350 m, respectively. The estimates found by MRPI are at the lower end of this range. One should, however, keep in mind that the dimensions by the rupture models are only rough estimates. Furthermore, varying stress drop values within the reservoir may produce differences in rupture lengths. Note also, that MRPI is limited to the horizontal projection of each event. Hence, the MRPI provides a lower bound estimate of the rupture length.

An interesting observation following from our results is derived from the direction of rupture propagation. The four analyzed ruptures from the Basel reservoir show unilateral behavior and break mainly from the southeast toward the northwest. This is the direction from the periphery of the stimulated volume toward the open borehole (see Figure 9). They are also the largest events that occurred during the experiment. These findings are consistent with the observation that in EGSs, large-magnitude events tend to occur on the edges of the stimulated volume (Majer et al., 2007). Goertz-Allmann and Wiemer (2013) propose a geomechanical model that explains this observation based on the inverse relationship between the seismic *b*-value and differential stress.

The observations mentioned above (by Majer et al. [2007] and ours) seem to corroborate the recently proposed idea that induced events are more probable to occur on preexisting faults if the potential rupture surface lies nearly completely within the stimulated volume (Shapiro et al., 2011). The authors derived this hypothesis from observing an underrepresentation of large-magnitude induced events in the frequency-magnitude statistics. They propose a simple physical justification of the hypothesis based on a balance of the surface-integrated friction force and tangential traction acting along the complete potential rupture surface. This hypothesis includes the possibility of large rupture surfaces spanning a range from an internal region to the far periphery of the stimulated volume. Such rupture surfaces would be sufficiently perturbed by a fluid injection at the moment when a sufficient pressure variation has reached potential rupture domains farthest from the injection source. It is very probable that such a far-distant domain of the potential rupture surface would then correspond to the hypocenter of a large induced event (because the rupture could start immediately after this domain has been perturbed). Thus, the rupture would be highly probable to propagate backward to the injection source. Our results on the rupture propagation at the Basel location agree well with this model. Moreover, our observations and the described scenario are in good agreement with one more known observation reported by Majer et al. (2007): The largest events tend to occur at the end of the injection period or even after its termination. It is clear that exactly this must be the case for large ruptures propagating from the rim of the stimulated volume toward the injection source.

Note, however, that there are also publications reporting a broad spatial distribution of large-magnitude events in microseismic clouds (i.e., Asanuma et al., 2005; Mukuhira et al., 2013).

CONCLUSIONS

We show the capability of the MRPI technique to image rupture processes in microseismic reservoirs for relatively large events and to distinguish between synthetic events such as point sources and unilateral and bilateral ruptures of different rupture directions.

The rupture parameters nucleation point (hypocenter), rupture orientation, direction, and length can be estimated. However, using a realistic, sparsely distributed monitoring system, the rupture orientation is biased.

Based on an adequate velocity model, we image the rupture of the four largest, $M_L = 3.1$–3.4 microseismic events at Basel and estimate their rupture parameters. The rupture orientations found here are reasonably consistent with the orientations of one of the nodal planes of the fault-plane solutions from independent FPS studies.

Moreover, our method allows to resolve the ambiguity of the nodal planes and determine the actual fault plane. The rupture dimensions we find are in the same range as the estimates computed from utilizing the stress-drop estimates from another independent stress-drop study at Basel and combining them with an appropriate rupture model.

Additionally, our results indicate that the rupture nucleation points lie further away from the well than the rupture termination points, which suggests that the largest induced events at Basel tend to rupture toward the injection point.

REFERENCES

Allmann, B. P., and P. M. Shearer, 2007, A high-frequency secondary event during the 2004 Parkfield earthquake: Science, **318**, 1279–1283, doi: 10.1126/science.1146537.

Asanuma, H., H. Nozaki, H. Niitsuma, and D. Wyborn, 2005, Interpretation of microseismic events with larger magnitude collected at Cooper Basin, Australia: Transactions of the Geothermal Resource Council, **29**, 87–91.

Bayer, B., R. Kind, M. Hoffmann, X. Yuan, and T. Meier, 2012, Tracking unilateral earthquake rupture by P-wave polarization analysis: Geophysical Journal International, **188**, 1141–1153, doi: 10.1111/j.1365-246X.2011.05304.x.

Brune, J., 1970, Tectonic stress and the spectra of seismic shear waves from earthquakes: Journal of Geophysical Research, **75**, 4997–5009, doi: 10.1029/JB075i026p04997.

Deichmann, N., and D. Giardini, 2009, Earthquakes induced by the stimulation of an enhanced geothermal system below Basel (Switzerland): Seismological Research Letters, **80**, 784–798, doi: 10.1785/gssrl.80.5.784.

Dyer, B. C., U. Schanz, T. Spillmann, F. Ladner, and M. O. Häring, 2010, Application of microseismic multiplet analysis to the Basel geothermal reservoir stimulation events: Geophysical Prospecting, **58**, 791–807, doi: 10.1111/j.1365-2478.2010.00902.x.

Eshelby, J. D., 1957, The determination of the elastic field of an ellipsoidal inclusion, and related problems: Proceedings of the Royal Society of London: Series A, **241**, 376–396.

Goertz-Allmann, B. P., A. Goertz, and S. Wiemer, 2011a, Stress drop variations of induced earthquakes at the Basel geothermal site: Geophysical Research Letters, **38**, L09308, doi: 10.1029/2011GL047498.

Goertz-Allmann, B. P., B. Edwards, F. Bethmann, N. Deichmann, J. Clinton, D. Fäh, and D. Giardini, 2011b, A new empirical magnitude scaling relation for Switzerland: Bulletin of the Seismological Society of America, **101**, 3088–3095.

Goertz-Allmann, B. P., and S. Wiemer, 2013, Geomechanical modeling of induced seismicity source parameters and implications for seismic hazard assessment: Geophysics, **78**, no. 1, KS25–KS39, doi: 10.1190/geo2012-0102.1.

Häring, M. O., U. Schanz, F. Ladner, and B. C. Dyer, 2008, Characterization of the Basel 1 enhanced geothermal system: Geothermics, **37**, 469–495, doi: 10.1016/j.geothermics.2008.06.002.

Ishii, M., P. M. Shearer, H. Houston, and J. E. Vidale, 2007, Telseseismic P wave imaging of the 26 December 2004 Sumatra-Andaman and 28 March 2005 Sumatra earthquake ruptures using the Hi-net array: Journal of Geophysical Research, **112**, B11307, doi: 10.1029/2006JB004700.

Jost, M. L., T. Büsselberg, Ö. Jost, and H.-P. Harjes, 1998, Source parameters of injection-induced microearthquakes at 9-km depth at the KTB deep drilling site, Germany: Bulletin of the Seismological Society of America, **88**, 815–832.

Kao, H., and S.-J. Shan, 2007, Rapid identification of earthquake rupture plane using source-scanning algorithm: Geophysical Journal International, **168**, 1011–1020, doi: 10.1111/j.1365-246X.2006.03271.x.

Kiser, E., and M. Ishii, 2011, The 2010 Mw 8.8 Chile earthquake: Triggering on multiple segments and frequency-dependent rupture behavior: Geophysical Research Letters, **38**, L07301, doi: 10.1029/2011GL047140.

Kiser, E., and M. Ishii, 2012, The March 11, 2011 Tohoku-oki earthquake and cascading failure of the plate interface: Geophysical Research Letters, **39**, L00G25, doi: 10.1029/2012GL051170.

Knopoff, L., 1958, Energy release in earthquakes: Geophysical Journal of the Royal Astronomical Society, **1**, 44–52, doi: 10.1111/j.1365-246X.1958.tb00033.x.

Krüger, F., and M. Ohrnberger, 2005, Spatio-temporal source characteristics of the 26 December 2004 Sumatra earthquake as imaged by teleseismic broadband arrays: Geophysical Research Letters, **32**, L24312, doi: 10.1029/2005GL023939.

Kummerow, J., S. A. Shapiro, H. Asanuma, and M. Häring, 2011, Application of an arrival time and cross correlation value-based location algorithm to the Basel 1 microseismic data: 73rd Annual International Conference and Exhibition, EAGE, Extended Abstracts, P193.

Madariaga, R., 1976, Dynamics of an expanding circular fault: Bulletin of the Seismological Society of America, **66**, 639–666.

Majer, E. L., R. Baria, M. Stark, S. Oates, J. Bommer, B. Smith, and H. Asanuma, 2007, Induced seismicity associated with enhanced geothermal systems: Geothermics, **36**, 185–222, doi: 10.1016/j.geothermics.2007.03.003.

Mukuhira, y., H. Asanuma, H. Niitsuma, and M. O. Häring, 2013, Characteristics of large-magnitude microseismic events recorded during and after stimulation of a geothermal reservoir at Basel, Switzerland: Geothermics, **45**, 1–17, doi: 10.1016/j.geothermics.2012.07.005.

Saenger, E. H., N. Gold, and S. A. Shapiro, 2000, Modeling the propagation of elastic waves using a modified finite-difference grid: Wave Motion, **31**, 77–92, doi: 10.1016/S0165-2125(99)00023-2.

Shapiro, S. A., O. Krüger, , C. Dinske, and C. Langenbruch, 2011, Magnitudes of induced earthquakes and geometric scales of fluid-stimulated rock volumes: Geophysics, **76**, no. 6, WC55–WC63, doi: 10.1190/geo2010-0349.1.

Walker, K. T., and P. M. Shearer, 2009, Illuminating the near-sonic ruptur velocities of the intracontinental Kokoxili M_w 7.8 and Denali fault M_w 7.9 strike-slip earthquakes with global P wave back projection imaging: Journal of Geophysical Research, **114**, B02304, doi: 10.1029/2009JG000990.